JGR Oceans

RESEARCH ARTICLE

10.1029/2023JC020365

Destratifying and Restratifying Instabilities During Down-Front Wind Events: A Case Study in the Irminger Sea

F. W. Goldsworth[1,2], **H. L. Johnson**[3], **D. P. Marshall**[1], **and I. A. Le Bras**[4]

[1]AOPP, Department of Physics, University of Oxford, Oxford, UK, [2]Oxford NERC Environmental Research DTP, Oxford, UK, [3]Deparment of Earth Science, University of Oxford, Oxford, UK, [4]Woods Hole Oceanographic Institution, Woods Hole, MA, USA

Key Points:

- Gravitational and symmetric instabilities deepen the mixed layer proportional to the square root of time-integrated down-front wind stress
- Time-mean water mass transformation rates are linearly proportional to the time-integrated down-front wind stress
- Down-front winds transform 0.9–1.0 Sv of buoyant surface water into East Greenland Coastal Current water between November and April

Supporting Information:

Supporting Information may be found in the online version of this article.

Correspondence to:

F. W. Goldsworth,
fraser.goldsworth@physics.ox.ac.uk

Citation:

Goldsworth, F. W., Johnson, H. L., Marshall, D. P., & Le Bras, I. A. (2024). Destratifying and restratifying instabilities during down-front wind events: A case study in the Irminger Sea. *Journal of Geophysical Research: Oceans*, *129*, e2023JC020365. https://doi.org/10.1029/2023JC020365

Received 17 AUG 2023
Accepted 22 JAN 2024

Author Contributions:

Conceptualization: F. W. Goldsworth, H. L. Johnson, D. P. Marshall, I. A. Le Bras
Data curation: F. W. Goldsworth, I. A. Le Bras
Formal analysis: F. W. Goldsworth
Funding acquisition: H. L. Johnson, D. P. Marshall, I. A. Le Bras
Investigation: F. W. Goldsworth, H. L. Johnson, D. P. Marshall, I. A. Le Bras
Methodology: F. W. Goldsworth, H. L. Johnson, D. P. Marshall, I. A. Le Bras
Resources: F. W. Goldsworth, H. L. Johnson, D. P. Marshall
Software: F. W. Goldsworth

Abstract Observations indicate that symmetric instability is active in the East Greenland Current during strong northerly wind events. Theoretical considerations suggest that mesoscale baroclinic instability may also be enhanced during these events. An ensemble of idealized numerical ocean models forced with northerly winds shows that the short time-scale response (from 10 days to 3 weeks) to the increased baroclinicity of the flow is the excitation of symmetric instability, which sets the potential vorticity of the flow to zero. The high latitude of the current means that the zero potential vorticity state has low stratification, and symmetric instability destratifies the water column. On longer time scales (greater than 4 weeks), baroclinic instability is excited and the associated slumping of isopycnals restratifies the water column. Eddy-resolving models that fail to resolve the submesoscale should consider using submesoscale parameterizations to prevent the formation of overly stratified frontal systems following down-front wind events. The mixed layer in the current deepens at a rate proportional to the square root of the time-integrated wind stress. Peak water mass transformation rates vary linearly with the time-integrated wind stress. Mixing rates saturate at high wind stresses during wind events of a fixed duration which means increasing the peak wind stress in an event leads to no extra mixing. Using ERA5 reanalysis data we estimate that between 0.9 Sv and 1.0 Sv of East Greenland Coastal Current Waters are produced by mixing with lighter surface waters during wintertime due to down-front wind events. Similar amounts of East Greenland-Irminger Current water are produced.

Plain Language Summary Symmetric instability is a process that leads to the mixing of waters with different densities. Observations show that in winter, when winds blow from the north, along the coast of Greenland, symmetric instability occurs; however, observations are limited which makes it difficult to understand the effect of the instability on the ocean currents in the region. We test the hypothesis that symmetric instability leads to the production of dense waters which are known to form in the region and contribute to the Atlantic Meridional Overturning Circulation (or "ocean conveyor" (Broecker, 1991, https://doi.org/10.5670/oceanog.1991.07)). We find that symmetric instability makes waters at the ocean surface denser, so that subsequent cooling can make them dense enough to sink to the deep ocean. A second type of instability, called baroclinic instability leads to the development of a fresh water "lid" which sits on top of the newly formed water masses, isolating them from the atmosphere. State of the art climate models don't resolve symmetric instability which means they may not get the density structure in the sub-polar North Atlantic correct, which could lead to errors in ocean heat transports which are important in determining the Earth's climate.

1. Introduction

The Irminger Sea is the region of the North Atlantic that sits between the East Coast of Greenland, the West Coast of Iceland and the Reykjanes Ridge. It has recently been revealed by OSNAP observations to be an important region in the formation of dense North Atlantic Deep Waters which make up the lower limb of the AMOC (Lozier et al., 2019). This finding came as a surprise to many, with many ocean and coupled climate models suggesting deep water formation primarily occurs in the adjacent Labrador Sea (Hirschi et al., 2020). As such, there has been a renewed interest in processes that may enhance deep water formation in the Eastern Sub-polar North Atlantic Ocean (de Jong & de Steur, 2016; Gutjahr et al., 2022; Josey et al., 2019; Le Bras et al., 2022). One such process is symmetric instability which produces submesoscale shear capable of triggering diapycnal mixing (Taylor & Ferrari, 2009). Observations indicate that it is excited in the East Greenland Current system during strong northerly wind events (Le Bras et al., 2022).

Supervision: H. L. Johnson, D. P. Marshall, I. A. Le Bras
Visualization: F. W. Goldsworth
Writing – original draft: F. W. Goldsworth, I. A. Le Bras
Writing – review & editing: F. W. Goldsworth, H. L. Johnson, D. P. Marshall, I. A. Le Bras

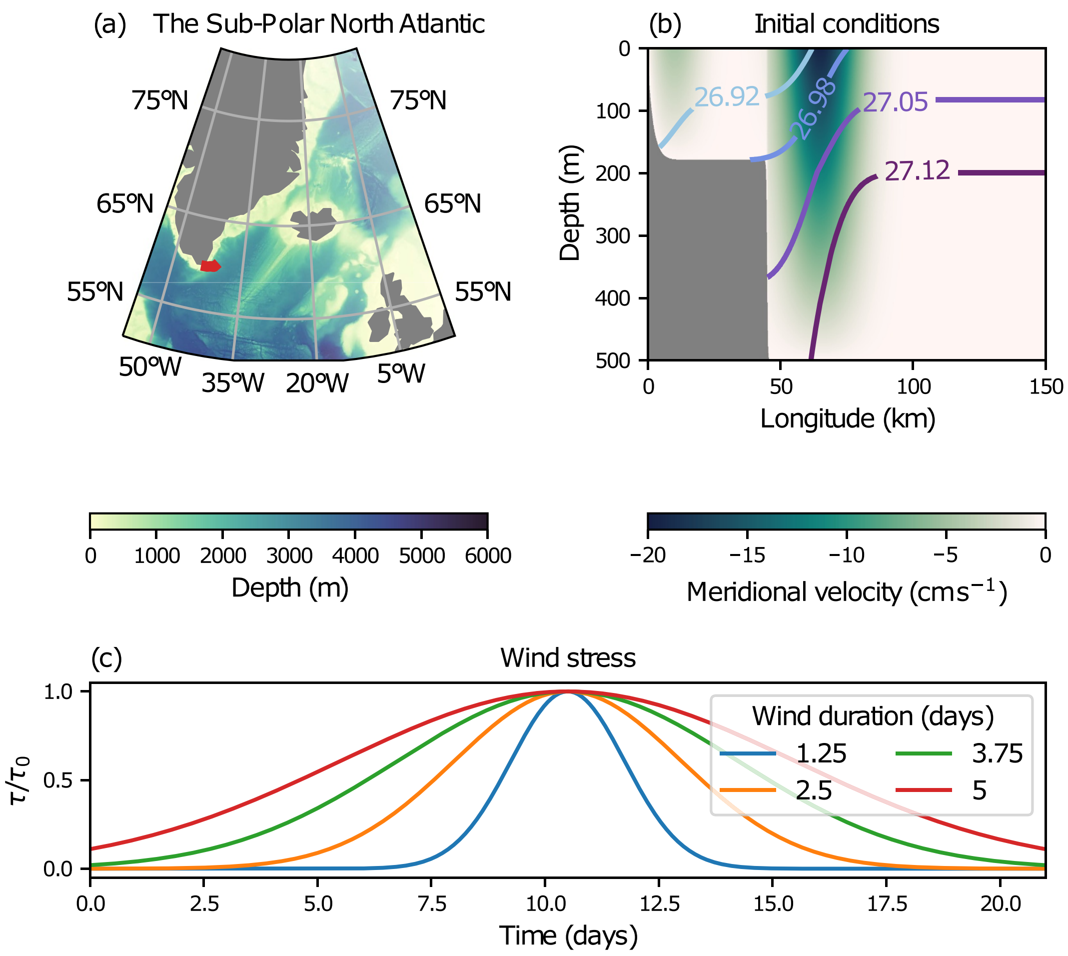

Figure 1. (a) The bathymetry of the Sub-Polar North Atlantic (GEBCO Compilation Group, 2020). Red line indicates the OSNAP section which the initial conditions and wind forcing used in our models are based on. (b) The density and velocity structure used to initialize the idealized models. (c) The different wind stresses used to force the models.

The East Greenland Current system consists of two surface intensified western boundary currents within the Irminger Sea (see Figure 1). They flow southwards along the east coast of Greenland, with the East Greenland Coastal Current on the landward side, and the East Greenland-Irminger Current sitting on the seaward side. The combined volume transport is around 18 Sv with peak speeds of around 20 cm s^{-1} found in the Irminger Current (Daniault et al., 2011; Le Bras et al., 2018; Talley et al., 2011a, 2011b). When a strong northerly wind blows over the current, outcropping isopycnals experience an Ekman transport toward the coast making them steeper (Figure 2). If they become sufficiently steep there may be an imbalance between the inertia, Coriolis and buoyancy forces acting on the flow (Thomas & Lee, 2005): we can show that in the Northern Hemisphere this is identical to the potential vorticity of the flow becoming negative (Ertel, 1942; Hoskins, 1974; Stone, 1966). Note that in this work we will use the classical definition of symmetric instability (Hoskins, 1974) rather than the energetic definition of Thomas and Lee (2005) – for further information see chapter two of F. W. Goldsworth (2022). For a current in thermal wind balance, potential vorticity, Q, is given by

$$Q = \left(f + \frac{\partial V}{\partial x}\right)\frac{\partial b}{\partial z} - \frac{1}{f}\left(\frac{\partial b}{\partial x}\right)^2, \tag{1}$$

where f is planetary vorticity, V is velocity, b is buoyancy, and x is the across stream and z the vertical coordinate of the flow. Note how in the Northern Hemisphere the final term of the equation is always negative, meaning increasing baroclinicity always leads to reduced symmetric stability (Haine & Marshall, 1998).

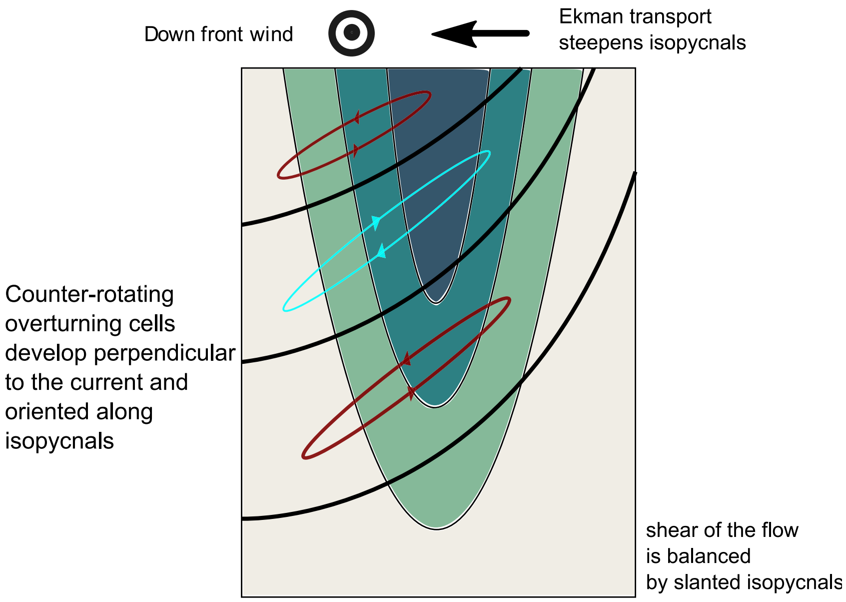

Figure 2. Schematic showing generation of slantwise overturning cells during a down-front wind event. Northerly winds blow along the current leading to a westward Ekman transport of outcropping isopycnals. This in turn reduces potential vorticity leading to the excitement of symmetric instability in regions where the potential vorticity is negative. Symmetric instability is characterized by stacked, counter-rotating overturning cells which orient themselves almost parallel to isopycnals. Background color depicts velocity, black lines isopycnals, and ellipses represent overturning cells.

The effect of symmetric instability is to produce slantwise convection, where overturning cells develop in a region of negative potential vorticity oriented almost parallel to isopycnals (Emanuel, 1994). The along-isopycnal scale of the cells is typically set by the width of the negative potential vorticity region whereas the across-isopycnal scale is set by both the rate of turbulent mixing, which acts to erode small scale overturning motions, and the stratification, which prohibits the formation of tall overturning cells (Plougonven & Zeitlin, 2009).

Symmetric instability has a dual character in that it can lead to either restratificaiton or destratification depending on the environment in which it occurs. When the overturning cells mix waters from the thermocline with waters from the base of the mixed layer, the mixed layer can become restratified (Bachman et al., 2017; Taylor & Ferrari, 2009); however, diapycnal mixing can be produced by shear instabilities that grow at the interfaces between overturning cells, which can lead to destratification too (Taylor & Ferrari, 2009).

Studies of Ekman induced symmetric instability in the sub-polar North Atlantic highlight this dual character. Straneo et al. (2002) found that wind-driven Ekman buoyancy fluxes over the Labrador Sea can be around a third of the size of the air-sea buoyancy flux, and concluded that symmetric instability should be taken into account when modeling deep water formation in the region, as slantwise convective cells can penetrate deeper than the upright convective cells that result from gravitational instability. More recently, Clément et al. (2023) found that the restratifying effect of symmetric instability and mixed layer eddies are responsible for the cessation of deep convection in the Labrador Sea. Ongoing modeling work is being carried out by Shu (2023) investigating symmetric instability and baroclinic instabilities in the region. Similarly to Clément et al. (2023) they see the formation of mixed layer eddies; however they also see symmetric instability destratifying the mixed layer. Spall and Thomas (2016) investigate the effect of down-front winds in an idealized model of a buoyant coastal plume, similar to the East Greenland Current. They force their models with a uniform meridional wind stress which is ramped up over 7 days and then held constant. They observe both symmetric instability and baroclinic instability, which act together to produce water mass transformations.

Observations of Ekman driven symmetric instability in the East Greenland Current producing a deeply penetrating low potential vorticity layer (Le Bras et al., 2022), coupled with our understanding of symmetric instability's ability to impact stratification (Taylor & Ferrari, 2009; Spall & Thomas, 2016, for example) raise questions about how much water mass transformation is driven by down-front wind events, and whether these highly seasonal events could be a source of AMOC variability. These questions are incredibly difficult to answer with sparse observations, and so here we will use idealized models to tackle them. The work of Spall and Thomas (2016) lays the foundations for addressing the above questions; however, their study design means it is only able to partially answer them. In their simulations, the forcing is held constant after the first 7 days of model integration. This means both potential vorticity and buoyancy are constantly being extracted from the flow, and the models will only equilibriate to a pseudo-steady state in which instability will constantly be excited. Therefore, estimates of mixing at later times in their integrations may be either overestimates or underestimates, depending upon whether the preconditioning by the wind stress at earlier times enhances or suppresses subsequent mixing. To estimate the effect of a wind event on mixing, we must model it as just that—an isolated event, with a wind stress which is ramped up and down to some characteristic value over a characteristic period of time.

In this work we address.

1. How symmetric and mesoscale baroclinic instabilities alter the mean structure of the East Greenland Current following down-front wind events;
2. The role of mesoscale baroclinic and submesoscale symmetric instabilities in producing diapycnal mixing during down-front wind events;
3. Approaches to parameterizing symmetric instability in coarse resolution models that fail to resolve the process.

In Section 2 we describe the suite of idealized models that underpin this study. In Section 3 we examine the effects of symmetric and mesoscale baroclinic instabilities on the structure of the (modeled) East Greenland Current following down-front wind events. In Section 4 we take a more quantitative look at the depth of the low potential vorticity layer and water mass transformation rates, before examining the implications for numerical climate models in Section 5. Finally, in Section 6 we summarize our results and make concluding remarks.

2. The Models

We integrate an ensemble of idealized models of the East Greenland current based on two different configurations of the MITgcm (Campin et al., 2022; Marshall et al., 1997). The first configuration is a non-hydrostatic two-dimensional model that is symmetric (periodic) in the along-stream direction. The domain is 150 km wide in the horizontal (across-stream) direction and 500 m deep. The horizontal and vertical grid spacings are set to 25 m and 1 m, respectively. The resolution was chosen to be high enough that small scale shear instabilities can be at least partially resolved (Griffiths, 2003; Yankovsky & Legg, 2019). The time step is set to 2 s and the models are integrated for a total of 21 days, with a subset of the ensemble integrated for 84 days.

This first configuration allows us to probe the fine-scale dynamics that occur during down-front wind events; however, the two-dimensional nature of the models prohibits the development of baroclinic instability which grows in the along stream direction (Stone, 1966). Given the high baroclinicity of the current system, it is plausible that mesoscale baroclinic instability will have a material effect on the dynamics. In order to resolve mesoscale baroclinic instability we also integrate a second set of model configurations which compromise on resolution but can be run in either a two-dimensional or three-dimensional setup.

This second configuration is hydrostatic and has a horizontal resolution of 200 m. In the three-dimensional setup the model domain has a meridional extent of 50 km, with periodic meridional boundaries. The time step is set to 4 s and the model is integrated for a total of 84 days. The model setup is otherwise identical to the non-hydrostatic configuration. A summary of the model integrations is shown in Table 1.

Both configurations are sited on an f-plane with f set to $1.26 \times 10^{-4}\ \mathrm{s}^{-1}$, corresponding to a latitude of 60°N. At the surface, a rigid lid boundary condition is employed, with the lateral and bottom boundaries set to be free-slip. The model has sloping bathymetry, which can be seen in Figure 1b. The model is initialized in thermal wind balance, with the velocity field and density profiles also shown in Figure 1b. Both of these fields are based on observations from the OSNAP array (Le Bras et al., 2022).

A linear equation of state is used, with a reference density of 1,027 kg m^{-3}, a thermal expansion coefficient of $2 \times 10^{-4}\ \mathrm{K}^{-1}$, and constant salinity. The thermal diffusion coefficient is set to $1 \times 10^{-5}\ \mathrm{m}^2\ \mathrm{s}^{-1}$. A second order-moment Prather advection scheme with a flux limiter is employed (Prather, 1986). Momentum dissipation is provided by an adaptive biharmonic lateral Smagorinsky viscosity and a vertical Laplacian viscosity of $4 \times 10^{-4}\ \mathrm{m}^2\ \mathrm{s}^{-1}$ (Griffies & Hallberg, 2000; Smagorinsky, 1963). The biharmonic viscosity is chosen to ensure dissipation occurs as close to the grid-scale as possible.

Table 1

Table Showing Parameters Used in the Different Model Integrations. τ_0 is the Maximum Down-Front Wind Stress. δ_t is the Wind Event Duration

Run	τ_0 (N m^{-2})	δ_t (days)	ΔX (m)	Pressure	Dimensions	Duration (days)
Standard 2D	0.5	2.5	25	NH	2D	84
Standard 3D	0.5	2.5	200	H	3D	84
Coarse 2D	0.5	2.5	200	H	2D	84
Ensemble	0–0.75	0–5	25	NH	2D	21

Note. ΔX is the model resolution. Pressure identifies whether the model was integrated in non-hydrostatic (NH) or hydrostatic (H) mode. Dimensions identifies whether the model was two-dimensional (2D) or three-dimensional (3D). Duration specifies the model integration time.

The models are forced using a time-varying, along-stream wind stress. The stress is spatially uniform and temporally Gaussian, taking the form

$$\tau_y = \tau_0 e^{-(t-t_{mid})^2/2\delta_t^2}, \qquad (2)$$

where τ_0 is the maximum wind stress, t_{mid} is the time at which the wind stress peaks and δ_t is the duration of the wind event. We integrate the non-hydrostatic configuration using 10 different values of τ_0 ranging linearly from 0 N m^{-2} to -0.75 N m^{-2} and four different values of δ_t ranging linearly from 1.25 to 5 days, giving 37 different ensemble members (when the wind stress is zero it doesn't matter how long the wind event is meaning there are only $40 - 3 = 37$ unique ensemble members.) A sketch of the wind forcing is show in Figure 1c. For comparison, the down-front wind events observed by Le Bras et al. (2022) had a typical duration of 1–2 days and a peak down-front wind stress of between ~1.0 N m^{-2} and ~2.0 N m^{-2}. Our models become numerically unstable when forced with stresses over 1 N m^{-2}, hence we use lower peak stresses here. In all integrations t_{mid} is set to 10.5 days.

We define the set of standard integrations as those in which $\tau_0 = -0.5$ N m^{-2} and $\delta_t = 2.5$ days. This set consists of a hydrostatic and non-hydrostatic two-dimensional integration, and a non-hydrostatic three-dimensional integration. Each of these models is integrated for 84 days.

In some of the model fields plotted here, thin horizontal and vertical lines are present. Investigation of their locations suggests they are a result of sharp "lego-like" bathymetry in the models. As far as we are aware, the features only come to prominence in fields involving derivatives and they have no effect on the large scale dynamics.

3. Instabilities and the Background Flow

3.1. Symmetric Instability

We first investigate the response to down-front winds in the standard two-dimensional model setup, in which symmetric and gravitational instabilities may be excited, but in which mesoscale baroclinic instability is not able to develop.

Examining the isopycnals plotted in Figure 3a, we see how after 1 week of down-front wind forcing there is an Ekman transport of surface waters toward the shelf, leading to a steepening of isopycnal surfaces. In panels (a) and (d) we see how both the potential vorticity and stratification are made negative near the surface, rendering the flow unstable to both symmetric and gravitational instabilities. Figure 4 shows the fraction of wet grid points susceptible to each of these instabilities as a function of depth and time in the integration. Note that gravitational instability is dominant in the surface whereas symmetric instability dominates below around 15 m. The spatial structure of potential vorticity, stratification and density (as shown in Figure 3) is very similar after three and 5 weeks, implying that symmetric instability is largely inactive during the time period following the wind event.

In panels (b) and (e) of Figure 3 we see a deeply penetrating low potential vorticity layer, which has incredibly low stratification. The low stratification of this low potential vorticity layer makes distinguishing it from the conventionally defined convectively mixed layer difficult. The low potential vorticity layer we see here is deeper

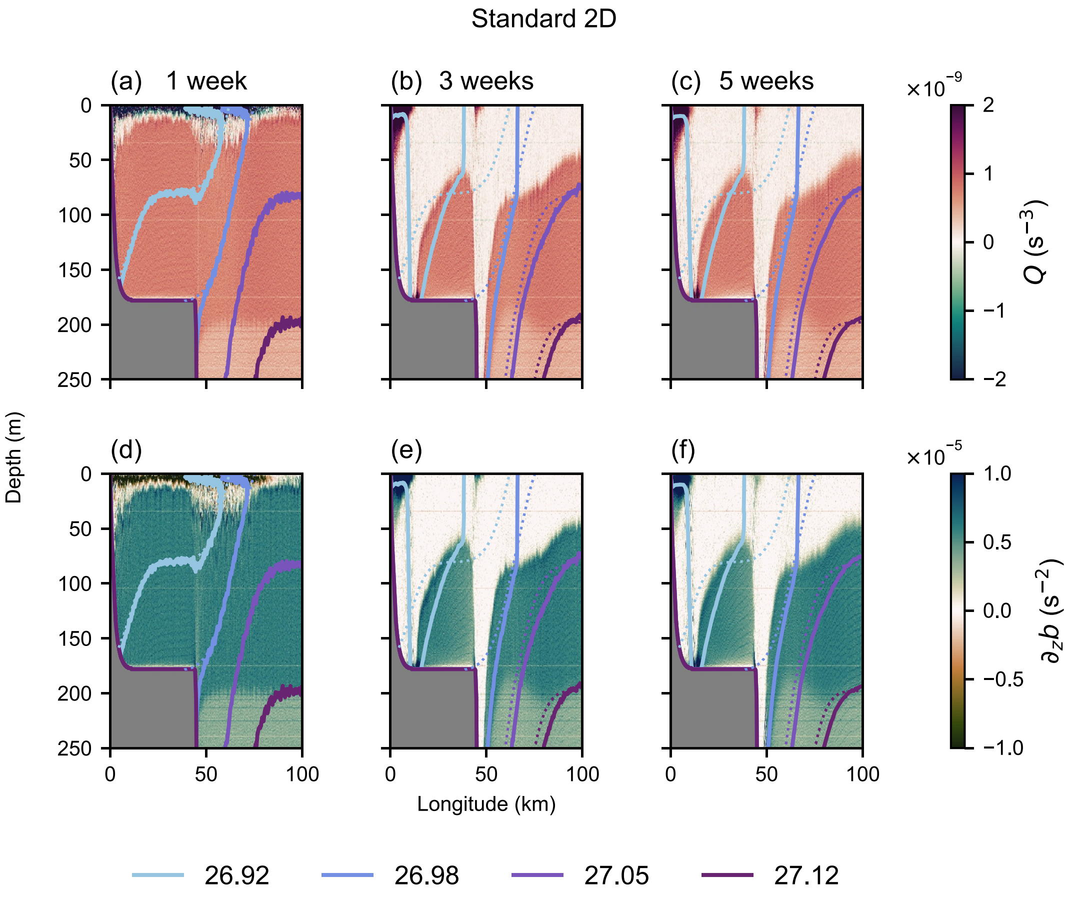

Figure 3. (a–c) Potential vorticity and (d–f) Stratification in the standard non-hydrostatic two-dimensional model integration. Solid contours show isopycnals and dashed contours their initial locations. Columns correspond to the quantities after 1 week, 3 and 5 weeks.

on the anticyclonic (shore-ward) flanks of the currents—an effect seen in observations too (Le Bras et al., 2022). It arises as regions of anticyclonic relative vorticity are less stable to symmetric instability: note that this deepening is not a bathymetric effect.

That the instability sets the vertical stratification to zero contrasts with studies of the Kuroshio and Gulf Stream, where it is found that the water column is restratified following the excitement of symmetric instability (D'Asaro et al., 2011; Thomas et al., 2013); however, the finding is consistent with observations from the Sub-polar North Atlantic (Le Bras et al., 2022) and the theory of Haine and Marshall (1998). We hypothesize that these differences stem from differences in planetary vorticity at high and mid latitudes — large planetary vorticity at high latitudes means that a zero potential vorticity state *must* have low stratification too. As we will shortly see in Section 3.2 the absence of mesoscale baroclinic instability in our two-dimensional models also leads to reduced stratification in regions where symmetric instability has occurred. Furthermore, our model resolution is high enough to at least partially resolve shear instabilities at interfaces between overturning cells. These regions can become susceptible to gravitational instability, further contributing to the low stratification when our results are compared to coarser modeling studies (see for example Figure S2 in Supporting Information S1 which shows the stratification in the coarse two-dimensional model integration).

3.2. Mesoscale Baroclinic Instability

The isopycnal structure following the excitement of symmetric instability (as seen in Figure 3f) is highly baroclinic, especially in the surface 100 m. The steeply slanted isopycnals, although stable to symmetric instability, are unstable to baroclinic instability. Baroclinic modes grow in the along stream direction (Stone, 1966) meaning that

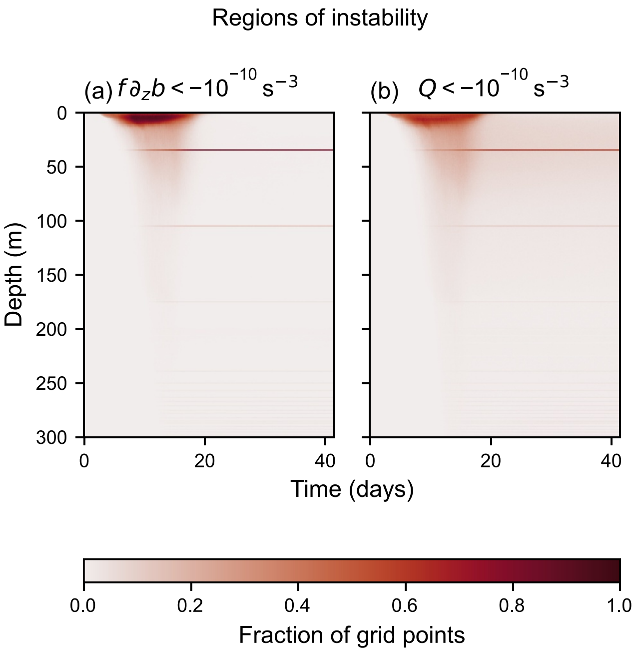

Figure 4. Fraction of wet grid cells susceptible to (a) gravitational instability and (b) symmetric instability as a function of depth and time in the standard non-hydrostatic two-dimensional model integration. Grid cells are taken to be susceptible to gravitational instability if $f\partial_z b < -10^{-10}$ s^{-3} and susceptible to symmetric instability if $Q < -10^{-10}$ s^{-3}—this is done to mask the effect of grid cells which are marginally stable and have small magnitude negative stratification and potential vorticity. The dark horizontal lines at 35 and 105 m of depth are due to the sharp bathymetry of the model. See the final paragraph of Section 2 for further detail.

they will not be resolved in our two-dimensional models with along stream symmetry. We will now examine output from the standard three-dimensional model run at a resolution of 200 m (standard 3D).

To ensure the resolution of this model is sufficient to capture the dynamics we are interested in, we also integrated a two-dimensional version of the model at the same resolution (coarse 2D) and compared its output with that of the finer non-hydrostatic reference simulation (standard 2D). We found that key fields such as potential vorticity and stratification are qualitatively similar and water mass transformation rates also look broadly similar (for more details see the supplementary information and Figures 6 and 8).

In Figure 5 we show meridionally averaged potential vorticity and stratification in the standard three-dimensional model integration. At early times (Figures 5a and 5d), these look very similar to the standard two-dimensional integration (Figures 3a and 3d), with the generation of negative potential vorticity and unstable stratification toward the surface. At 3 weeks, however, the low potential vorticity layer appears more diffuse and we see signs of restratification and the slumping of isopycnals at the surface, concentrated in the eastern part of the domain (Figures 5b and 5e). There is also restratification in the western part of the domain concentrated at the base of the inner shelf. Given the accompanying isopycnal slumping and the absence of the restratification in the two-dimensional models, we conclude that this is the effect of mesoscale baroclinic instability. After 5 weeks, the stratification at the surface in the eastern part of the domain has increased further, resulting in a highly stratified “lid” on top of the low potential vorticity waters below. Furthermore the potential vorticity in the low potential vorticity layer is increased, a result of mesoscale baroclinic eddies fluxing potential vorticity laterally and eroding potential vorticity gradients.

3.3. A Hierarchy of Instabilities

Other studies have found that baroclinic instability is more efficient at removing negative potential vorticity injected by Ekman buoyancy fluxes than symmetric instability (e.g., Haine & Marshall, 1998; Spall & Thomas, 2016). Our results do not contradict these previous works. In these studies, the authors force a front with constant winds in which a pseudo-steady state can be reached. In this steady state Ekman buoyancy fluxes are balanced by eddy fluxes. These eddies grow slowly over timescales given by the inverse of the Eady growth rate. During the initial stages of wind events when the flow is highly baroclinic, there may be other faster growing processes which are capable of steadying the system. Indeed, when the flow is highly baroclinic, symmetric instability can have a larger growth rate than that of baroclinic instability (Stone, 1966).

In our model simulations, we subject currents to wind stresses that are ramped up and back down again. Compared to the Eady growth rate, however, this ramping up and down behaves more like an impulse forcing which steepens the isopycnals faster than the steepening can be counteracted by any of baroclinic, symmetric or gravitational instability. On the shortest time scales (less than around two weeks) gravitational instability is excited in regions where the isopycnal tilt exceeds 90°—see for example, Figure 3d which shows the isopycnal structure just as the wind event is starting to ramp up, and Figure 4a which shows the regions susceptible to gravitational instability over time. On intermediate time scales (from 10 days to 3 weeks) symmetric instability is excited in regions with negative potential vorticity (typically corresponding to isopycnal tilts in excess of around 5°)—this is illustrated very clearly in Figure 4b where we see a number of grid points at depth becoming susceptible to symmetric instability after around 10 days, earlier at the surface. And, finally, on long timescales (after around 4 weeks) mesoscale baroclinic instability will be excited—visible in the isopycnal slumping shown in Figure 5c. The transition from gravitational to symmetric instability and symmetric to baroclinic instability will occur when their growth rates are of similar orders of magnitude for the isopycnal structure of the time (Stamper & Taylor, 2017). The transition from gravitational to symmetric instability can be expected to occur for a Richardson number of

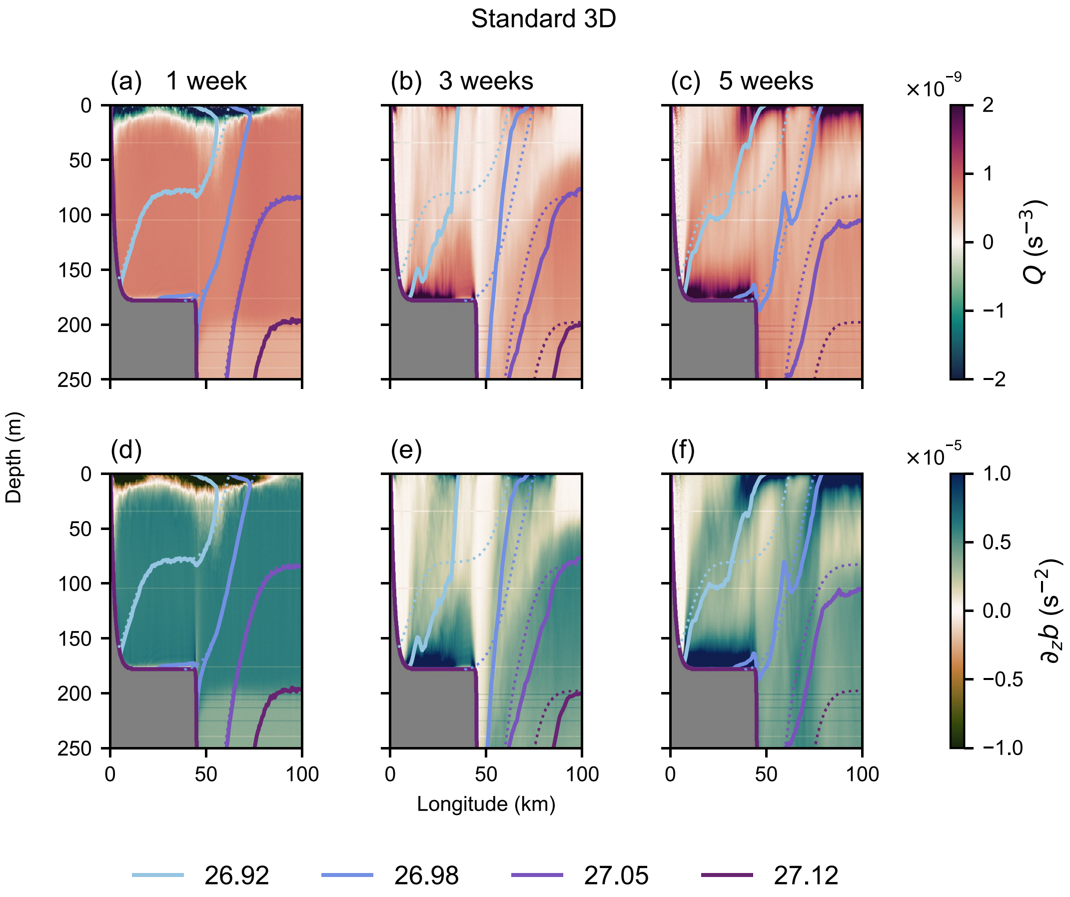

Figure 5. Evolution of meridionally averaged (a–c) potential vorticity and (d–f) stratification in the standard hydrostatic three-dimensional model integration. Solid contours show isopycnals and dashed contours their initial locations. Columns correspond to the quantities after 1 week, 3 and 5 weeks.

around one (Thomas et al., 2013), and for symmetric to baroclinic instability this corresponds to a Richardson number of 0.95 (Stamper & Taylor, 2017; Stone, 1966). In reality, all three instabilities will be growing concurrently and interacting with each other (Stamper & Taylor, 2017); however, thinking in terms of a hierarchy of instabilities is a useful abstraction.

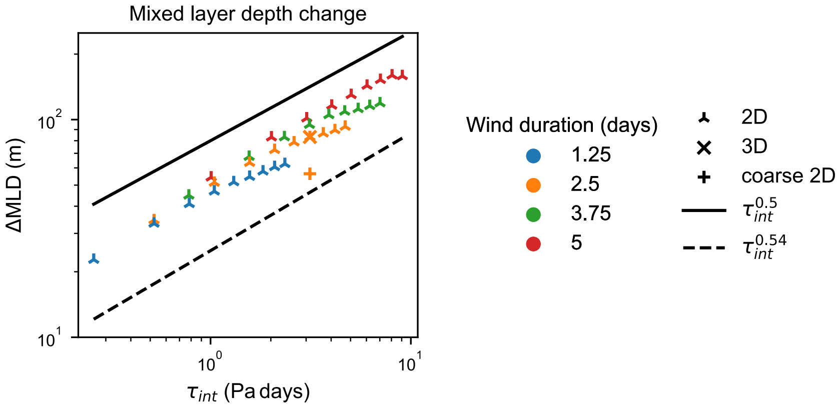

Figure 6. Spatially averaged change in mixed layer depth between day 0 and day 21, as a function of integrated wind stress. Both horizontal and vertical axes are logarithmic. Triagonal markers correspond to integrations from the 2D ensemble, the cross the standard 3D, and the plus the coarse 2D integrations. Colors show the duration of the wind event. The solid line shows the mixed layer depth scaling predicted by theory and the dashed line the scaling found across the 2D ensemble members.

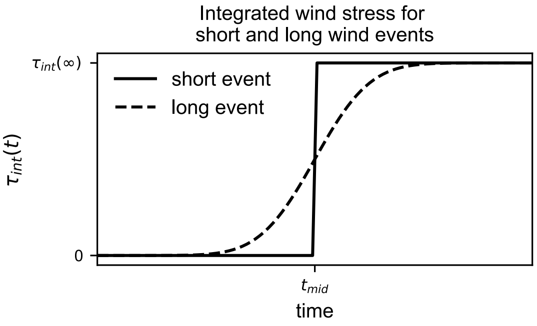

Figure 7. Integrated wind stress as a function of time for wind events with short and long durations. For short wind events (solid line) the wind stress resembles a step function, whereas for longer wind events (dashed line) the integrated wind stress varies more gradually.

4. Diapycnal Mixing

The results shown in Figure 3 suggest that down-front wind events may be a mechanism by which dense waters can be formed. We will now use our model ensemble to investigate the dependence of the low potential vorticity layer depth, and water mass transformation patterns, on the parameters of the down-front wind event.

4.1. Mixing Depth

Taylor and Ferrari (2010) propose a scaling for the depth of the low potential vorticity layer generated during down-front wind events. Assuming the only forcing comes from winds and that the initial depth of the low potential vorticity layer is zero, the scaling can be summarized as

$$\frac{\mathrm{d}H^2}{\mathrm{d}t} \propto B_{wind} \tag{3}$$

where H is the depth of the low potential vorticity layer and B_{wind} is the Ekman buoyancy flux induced by the down-front winds, and is given by

$$B_{wind} = -\frac{\tau_y \partial_x b}{\rho_0 f}. \tag{4}$$

Integrating Equation 3 under the assumption that $\partial_x b$ is approximately constant, we find that

$$H(t = t_{end}) \propto \tau_{int}^{1/2}, \tag{5}$$

where τ_{int} is the temporally integrated wind stress. As noted already, the low potential vorticity layer in our models, due to its low stratification, is almost indistinguishable from the mixed layer. If we assume the change in mixed layer depth is a result of the expansion of the low potential vorticity layer we would expect changes in mixed layer depth to scale with the square root of the integrated wind stress.

We define the mixed layer depth as the depth at which density changes by 0.05 kg m^{-3} relative to the surface density. In Figure 6 we show the change in mixed layer depth plotted against integrated wind stress for each member of our ensemble (note both axes are logarithmic). Performing a least squares regression on the ensemble data and using a t-test to estimate the confidence intervals, we find that the change in mixed layer depth scales with τ_{int} to the power of 0.54, with a 95% confidence interval of 0.49–0.58. This is remarkably consistent with the value of 0.5 predicted by idealized theory. Lines showing the 0.5 and 0.54 power laws are also shown in Figure 6a. Note how, for a given wind duration, the change in mixed layer depth starts to saturate as the wind strength is increased. This saturation suggests that the amount of mixing may be limited by the duration of the wind event. We can understand why this occurs as follows: if we relax the condition of $\partial_x b$ being constant, integrating Equations 3 and 4 by parts we find that

$$H^2(t) \propto \left(\tau_{int}(t)\partial_x b(t) - \int_{t'=t_0}^{t} \tau_{int}\left(t'\right) \frac{\partial^2 b}{\partial x \partial t'} \mathrm{d}t', \right) \tag{6}$$

where $\tau_{\text{int}}(t)$ is the wind stress integrated from $t' = t_0$ to $t' = t$. It is the integral in the above equation that causes deviations from the power law and, as such, we will refer to this as the "correction" term. For an infinitesimally short wind event, $\tau_{\text{int}}(t)$ is given by a step function (Figure 7). This means the integrand in Equation 6 will only be non-zero at times following the wind event. Evaluating Equation 6 for an infinitesimally short wind event we recover Equation 5 exactly.

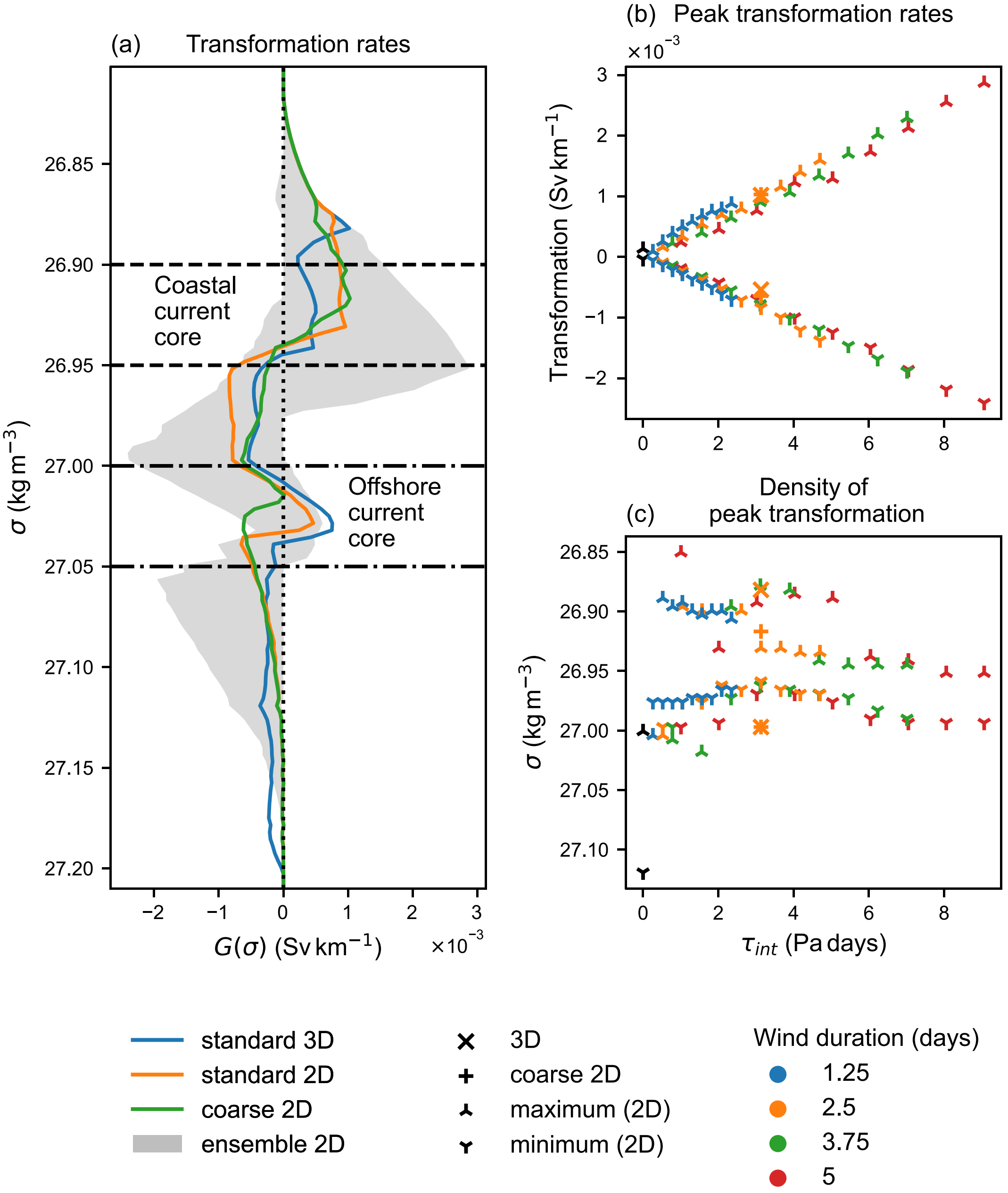

Figure 8. (a) Water mass transformation rates for the standard 3D (blue), standard 2D (orange) and coarse 2D (green) integrations. Gray envelope denotes the maximum and minimum transformation rates across the 2D ensemble. The plotted rates have the dimensions of transformation per unit length. To get the transformation in Sv the data should be multiplied by the length of the current, which for the East Greenland Current system is around 1,000 km. (b) The maximum (upward pointing triagonals) and minimum (downward pointing triagonals) water mass transformation rates as a function of integrated wind stress. (c) The densities of the maximum (upward pointing triagonals) and minimum (downward pointing triagonals) water mass transformation rates as a function of integrated wind stress. In panels (b) and (c) color corresponds to the duration of the wind event. In place of triagonals, the standard 3D model is represented by a cross and the coarse 2D model is represented by a plus.

For a longer wind event, $\tau_{\text{int}}(t)$ increases more gradually (Figure 7), meaning that the integrand is non-zero over a wider time interval. This means that, for a given wind strength, the "correction" term is larger, leading to larger deviations from the power law. Because of this, care should be taken when considering whether the power law scaling applies to longer or stronger wind events than those discussed here.

4.2. Water Mass Transformation

The water mass transformation framework of Walin (1982) allows us to quantify diapycnal volume fluxes (which represent the amount of diapycnal mixing) integrated along isopycnals. Consider a volume of size ΔV bounded above and below by isopycnals of density σ and $\sigma + \Delta\sigma$ respectively. In a closed domain, the only way the volume between the isopycnals can change is if there is a convergence or divergence of the diapycnal volume fluxes, G, integrated over the isopycnals. This quantity is often referred to as the water mass transformation rate. Mathematically we can write

$$\frac{\partial \Delta V}{\partial t} = G(\sigma) - G(\sigma + \Delta\sigma), \tag{7}$$

with positive values of G indicating a flux from lighter to denser water. The time mean fluxes, G, can be diagnosed from the instantaneous density field as follows.

1. Define density bins, and at the first and last time-step, bin grid cell volumes by their instantaneous density. Sum all the volumes in the bin to find $\Delta V\ (\sigma, t)$;
2. Subtract these values and divide by the elapsed time to find the time averaged value of $\partial_t \Delta V(\sigma)$;
3. Cumulatively integrate the time averaged value of $\partial_t \Delta V(\sigma)$ over density, with the boundary condition of $G\ (\sigma_{\max}) = 0$.

Thus we are able to find the time averaged $G(\sigma)$.

Figure 8a shows the time averaged water mass transformation rates in density space for the standard three-dimensional (blue) and two-dimensional integrations (orange), and the coarse two-dimensional control integration (green). The gray envelope displays the maximum and minimum transformation from the 2D ensemble of simulations. The coarse two-dimensional model (green) does a good job of representing the transformation close to the surface relative to its finer resolution counterpart (orange); however, transformation is suppressed at depth—in particular in the 27.00–27.05 kg m^{-3} density classes. This suggests that transformation rates in the standard 3D model are likely reasonable and possibly slightly underestimated.

The transformation rates have a double peak structure, with two maxima and two minima as a function of depth. Broadly speaking this means we have two density classes at which the transformation rates converge (are formed) and three density classes at which the transformation rates diverge (water masses are depleted). For the model integrations plotted, the lightest water mass formed has a density of between 26.90 kg m^{-3} and 26.95 kg m^{-3} with a deeper set of water masses formed between around 27.00 kg m^{-3} and 27.05 kg m^{-3}. Waters with density between these two classes are depleted, as are surface and deep waters. All models with non-negligible transformation rates have double transformation peaks. The lighter of these water mass classes corresponds to water masses in the core of the East Greenland Coastal Current between depths of 100 m and 200 m; whereas, the heavier water mass class corresponds to water masses in the core of the East Greenland-Irminger Current in the same depth range.

Comparing the standard two-dimensional (orange) and three-dimensional (blue) models, we see that mesoscale baroclinic instability suppresses water mass transformation near the surface, especially in the 26.90–26.95 kg m^{-3} class. This is likely a result of the restratifying effect of the mesoscale baroclinic instability. In the 27.00–27.05 kg m^{-3} density range there is enhanced downwelling. This corresponds to the density classes present on the inner shelf of the model, where we see enhanced restratification in the three-dimensional model (see Figure 5 for example).

Figure 8b shows how the maximum and minimum of the time averaged diapycnal volume fluxes vary with the integrated wind stress—the response is linear. The rates have both maxima and minima as at different depths the diapycnal volume flux may be toward either lighter or denser waters. Also shown on this panel are transformation rates from the coarse and three-dimensional models, which appear to follow the same relationship as the two-dimensional ones. Performing a linear regression over data points from the two-dimensional ensemble, and using a t-test to find the confidence intervals, we find that the maximum and minimum transformation rates scale as $(3.00 \pm 0.20) \times 10^{-4}$ Sv km^{-1} Pa^{-1} day^{-1} and $(-2.69 \pm 0.08) \times 10^{-4}$ Sv km^{-1} Pa^{-1} day^{-1}, respectively.

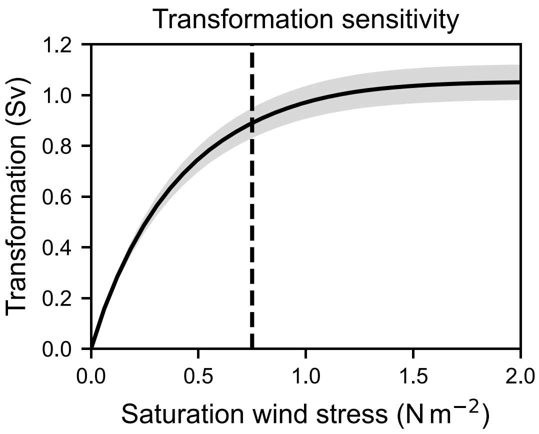

Figure 9. Wintertime transformation plotted as a function of the wind stress at which water mass transformation rates saturate. The true saturation wind stress in unknown; however, the dashed line shows the wind stress at 0.75 N m^{-2}, which puts a lower bound on the saturation wind stress. As such, it is likely that the true wintertime transformation rate into "East Greenland Coastal Current waters" at $\sigma \approx 26.95$ kg m^{-3} lies somewhere in the range 0.9–1.0 Sv. Shading shows the range of the transformation when calculated using the 95% confidence intervals on the transformation rate scaling factors previously calculated. We assume a current length of 200 km.

Figure 8c shows how the isopycnals of maximum and minimum transformation vary with the wind stress. Above a wind stress of approximately 3 Pa days, the isopycnals are unaffected by the integrated wind stress, with maximal densification close to the surface and the lightening of deeper waters. The maxima and minima sit directly above and below the lighter of the two water mass classes that are formed, meaning transformation between the upper water masses is greatest.

The linearity of the time-averaged transformation rates with respect to the integrated wind stress (Figure 8a) implies the volume of dense water formed by a wind event is directly proportional to the integrated wind stress. From this, we can estimate an upper bound on the average transformation rate over the course of a season. The average transformation rate will be given by the scaling of the peak transformation rate multiplied by the down-front wind stress integrated over a season (multiplied by 21 days and divided by the number of days in a season). This is an upper bound on the mixing as we expect the mixing rates to saturate as we go to larger wind stresses (similarly to how the changes in mixed layer depth saturate). Using ERA5 hourly data (Copernicus Climate Change Service, 2023; Hersbach et al., 2020) we calculate the zonal average of the meridional wind stress at 60°N between 43°W and 41°W for the months of November through April, from 2014 to 2018. We select observations with southerly wind stresses and integrate the resulting time series over the time dimension. We get a wintertime total integrated down-front wind stress of 30 Pa days. Assuming a current length (1,000 km is approximately the distance from the Denmark Strait to Cape Farewell at the Southern tip of Greenland) of 1,000 km and a scaling of 3×10^{-4} Sv km^{-1} Pa^{-1} day^{-1} (as previously calculated) we get a transformation rate of 1.0 Sv at $\sigma \approx 26.95$ kg m^{-3}.

For a given wind event duration, there will be a wind stress at which increasing the integrated wind stress does not lead to an increase in mixing—the linear relationship between water mass transformation rates and integrated wind stress will break down. Wind stresses over this threshold will cause the same amount of mixing as if the wind stress were *at* this threshold and so 1.0 Sv of water mass transformation will be an upper bound on the amount of mixing occurring in winter. We now attempt to estimate the wintertime mean transformation rate as a function of the wind stress at which the linear relationship breaks down—the saturation wind stress. We calculate the wintertime mean integrated wind stress from the same ERA5 data as used above; however, we set any wind stresses above a critical value, τ_{crit}, to be equal to τ_{crit}. We do this for a range of values of τ_{crit} and obtain the curve shown in Figure 9. Given that in this study we tested wind stresses up to 0.75 N m^{-2}, we expect winter-time wind events to produce *at least* 0.9 Sv of extra transformation across $\sigma \approx 26.95$ kg m^{-3} (this is the amount of transformation that occurs with a saturation wind stress of 0.75 N m^{-2})

The scaling used in estimating this seasonal range corresponds to peak transformation rates, which as we have just seen, describes the transformation of surface waters into "East Greenland Coastal Current waters." There will also be weaker transformation between denser water classes, and as Figure 8a shows, the order of magnitude will likely be similar.

In summary we expect down-front wind events to drive between 0.9 Sv and 1.0 Sv of water mass transformation across the 26.95 kg m^{-3} isopycnal during wintertime. To contextualize these numbers Gutjahr et al. (2022) found that, in the winter of 2020, Katabatic storms off the East coast of Greenland produced around 2.74 Sv of water mass transformation across the 27.6 kg m^{-3} isopycnal. At OSNAP East, AMOC strength is around 17 Sv and overturning anomalies are typically in the range ±8 Sv and the isopycnal of maximum overturning lies around 27.55 kg m^{-3} (Li et al., 2021; Lozier et al., 2019). This implies down-front wind events aren't leading directly to the formation of deep water, but may densify surface waters before they become North Atlantic Deep Waters. The temporal sparsity of down-front wind events suggest that they are unlikely to contribute to the time mean AMOC; however, it is plausible that they contribute to its variability. During summertime the down-front wind events tend to be less intense with the integrated wind stress summing to 16 Pa days, implying transformation rates are roughly halved at this time of year.

5. A Discussion on Parameterizations

Of key concern to those running, or using output from, numerical ocean models is how well the model in question captures these down-front wind events and whether they should be parameterized. This of course depends on the specific model configuration in question; however, we would like to make the following general remarks. If the model is not eddy resolving, it will certainly not be resolving symmetric instability. Attempting to parameterize the process is likely a waste of time as the areas where the parameterization is active will be a few grid cells thick at most and much bigger biases will likely be introduced by the lack of eddies in the model.

If, however, the model is eddy permitting or eddy resolving, a submesoscale parameterization would likely improve the representation of these down-front wind events. The parameterization of Bachman et al. (2017) may be effective—the parameterization makes use of the scaling proposed by Taylor and Ferrari (2010) which we showed here to be a good fit to our models. Comparing results from our models with a coarse resolution parameterized model is a clear next step in ascertaining whether parameterizations can adequately represent the submesoscale response to down-front wind events. If a good parameterization for the dynamics can be identified, it will become possible to examine the effect of down-front wind events over longer spatial and temporal scales. This will enable independent estimates of the amount of wintertime mixing induced by down-front wind events in the Sub-polar North Atlantic.

The above discussion pre-supposes that models can be defined as globally resolving either the mesoscale or submesoscale; however, this is not the case. The latitutidinal dependence of the Rossby deformation radius means that a model may be submesoscale resolving at the equator but barely even eddy resolving in the polar regions (Chelton et al., 1998). Dong et al. (2021) find that to resolve symmetric instability a resolution of only 2 km is needed in the tropics whereas a resolution as fine as 10 m is required in the high latitudes. This highlights the need for so-called "scale-aware" parameterizations which are able to autonomously adjust to the scales being locally resolved (Jansen et al., 2019). The parameterization of Jansen et al. (2019) focuses on the mesoscale but as the resolution of ocean models increases, it may be necessary to incorporate not just mesoscale, but submesoscale dynamics into such frameworks.

Large changes in the depth of the mixed layer following down-front wind events imply that they are a key process in setting the vertical stratification in the western boundary region of the Irminger Sea. The water mass transformation rates, however, show that this mixing occurs mostly within lighter surface waters, and does not lead to the direct formation of North Atlantic Deep Waters. It may be tempting to use this as evidence that the action of these events and symmetric instability can be neglected, but this is a simplistic interpretation of the results. Surface waters must lose a lot of buoyancy on their journey to the deep ocean, and symmetric instability may be one of several mechanisms that reduces it. Symmetric and gravitational instability excited during down-front wind events may then act to precondition surface waters before their subsequent transformation into deep waters.

This study didn't examine the role of down-front wind events in the lateral transport of fresh water and heat; however, given the intense eddy field and overturning cells that develop during these wind events, it seems plausible that the events could be responsible for large fluxes of freshwater away from the coast of Greenland and into the ocean interior. Further research is required to estimate the magnitude of these fluxes. If they are found to be significant, there would be an extra impetus to go to the expense of parameterizing the submesoscale instabilities excited during down-front wind events.

6. Conclusions

Observations show that strong northerly winds during spring and winter trigger the excitement of Ekman induced symmetric instability in the western boundary region of the Irminger Sea (Le Bras et al., 2022). This leads to the development of a deep low potential vorticity layer that sits below the conventionally defined convectively mixed layer (Le Bras et al., 2022; Taylor & Ferrari, 2010). The spatial sparsity of existing moored observations makes it difficult to determine the spatial structure of mixing and mixing rates during these wind events including accurately defining the extent of the low potential vorticity layer.

Using idealized models we were able to show that when a flow similar to the East Greenland Current system is forced with down-front winds, gravitational instability (up to around 4 days) and later symmetric instability (from 10 days to 3 weeks) are excited. This leads to the generation of a deep low potential vorticity layer with mesoscale baroclinic instability later restratifying waters at the surface (after around 4 weeks, c f. Stamper & Taylor, 2017).

This hierarchy of instabilities may lead to interesting insights if it were applied to the adjustment of Southern Ocean fronts to wind stress variability over different time scales.

The volume of waters transformed by a wind event (and hence the water mass transformation rates) vary linearly with the integrated wind stress. Using this fact in conjunction with ERA5 reanalysis products (Hersbach et al., 2020) we estimate that between around 0.9 Sv and 1.0 Sv of water mass transformation across the 26.95 kg m^{-3} isopycnal is produced by down-front wind events off the East coast of Greenland between November and April. The transformation is between light surface waters and East Greenland Coastal Current waters; however, there will also be formation of East Greenland-Irminger Current waters at a similar but slightly lower rate. Although we didn't explicitly calculate the variability of these rates, the temporal sparsity of these wind events may contribute to the ±8 Sv of AMOC variability observed at OSNAP East (Li et al., 2021).

Coarse resolution numerical ocean models do not resolve symmetric instability. We suggest that models that do not resolve mesoscale eddies should not worry about this omission as the absence of eddies is likely leading to much larger biases. Eddy permitting and eddy resolving models should, however, consider parameterizing the response of the ocean to down-front wind events, as failing to do so will lead to biases in the stratification. In particular the surface may end up overly stratified following down-front wind events. We suggest the parameterization of Bachman et al. (2017) may capture the dynamics well as it uses the scaling of Taylor and Ferrari (2010) which is effective at predicting mixed layer depths in the idealized models presented here. Future work should ascertain whether this is indeed the case. The severe latitudinal dependence of the ocean model resolution required to resolve symmetric instability also highlights the need for scale aware parameterizations of the submesoscale, capable of adjusting to the scale of the dynamics locally resolved (Dong et al., 2021; Jansen et al., 2019).

This work focused on diapycnal rather than along-isopycnal transports of heat and salt; however, this is a clear avenue for future research. Waters off the coast of Greenland are salinity stratified whereas in the interior of the Irminger Sea they are thermally stratified (Le Bras et al., 2022). Both symmetric instability and baroclinic eddies are effective at producing along-isopycnal mixing (Abernathey et al., 2022) and may be responsible for significant diahaline and diathermal transports, fluxing heat and salt between the boundary and the interior of the Irminger Sea, with potential implications for the stability of the AMOC to freshwater forcing (Swingedouw et al., 2022).

Data Availability Statement

All processed data and a selection of the raw data used in this study is available in F. Goldsworth et al. (2023). Code used for model integrations and subsequent analysis is available in F. Goldsworth (2023).

Acknowledgments

This research was funded in part by the Natural Environment Research Council Grants NE/L002612/1 (F. W. Goldsworth) and NE/T013494/1 (H. L. Johnson & D. P. Marshall). For the purpose of Open Access, the author has applied a CC BY public copyright licence to any Author Accepted Manuscript version arising from this submission. I. A. Le Bras acknowledges funding support from US National Science Foundation Grants OCE-2038481 and OCE-2122579. This work used the ARCHER2 UK National Supercomputing Service (https://www.archer2.ac.uk). We would also like to thank Andrew Coward for providing support with computational resources. The results contain modified Copernicus Climate Change Service information (2023). Neither the European Commission nor ECMWF is responsible for any use that may be made of the Copernicus information or data it contains. We are grateful for the comments of Elizabeth Yankovsky and an anonymous reviewer which helped to improve this work, and thank Tim Palmer and Alberto Naviera Garabato for their feedback on an early draft of this manuscript.

References

Abernathey, R., Gnanadesikan, A., Pradal, M.-A., & Sundermeyer, M. A. (2022). Chapter 9 - isopycnal mixing. In M. Meredith & A. Naveira Garabato (Eds.), *Ocean mixing* (pp. 215–256). Elsevier. https://doi.org/10.1016/B978-0-12-821512-8.00016-5

Bachman, S. D., Fox-Kemper, B., Taylor, J. R., & Thomas, L. N. (2017). Parameterization of frontal symmetric instabilities. I: Theory for resolved fronts. *Ocean Modelling*, *109*, 72–95. https://doi.org/10.1016/j.ocemod.2016.12.003

Broecker, W. S. (1991). The great ocean conveyor. *Oceanography*, *4*(2), 79–89. https://doi.org/10.5670/oceanog.1991.07

Campin, J.-M., Heimbach, P., Losch, M., Forget, G., Adcroft, A., & Deremble, B. (2022). MITgcm/MITgcm: checkpoint68i [Software]. zenodo. https://doi.org/10.5281/zenodo.6498956

Chelton, D. B., Deszoeke, R. A., Schlax, M. G., El Naggar, K., & Siwertz, N. (1998). Geographical variability of the first baroclinic Rossby radius of deformation. *Journal of Physical Oceanography*, *28*(3), 433–460. https://doi.org/10.1175/1520-0485(1998)028⟨0433:GVOTFB⟩2.0.CO;2

Clément, L., Frajka-Williams, E., Von Oppeln-Bronikowski, N., Goszczko, I., & De Young, B. (2023). Cessation of Labrador Sea convection triggered by distinct fresh and warm (sub)mesoscale flows. *Journal of Physical Oceanography*, *53*(8), 1959–1977. https://doi.org/10.1175/JPO-D-22-0178.1

Copernicus Climate Change Service. (2023). ERA5 hourly data on single levels from 1940 to present [Dataset]. Copernicus Climate Change Service (C3S) Climate Data Store (CDS). https://doi.org/10.24381/cds.adbb2d47

Daniault, N., Mercier, H., & Lherminier, P. (2011). The 1992-2009 transport variability of the East Greenland-Irminger Current at 60°N. *Geophysical Research Letters*, *38*(7), https://doi.org/10.1029/2011GL046863

D'Asaro, E., Lee, C., Rainville, L., Harcourt, R., & Thomas, L. N. (2011). Enhanced turbulence and energy dissipation at ocean fronts. *Science*, *332*(6027), 318–322. https://doi.org/10.1126/science.1201515

de Jong, M. F., & de Steur, L. (2016). Strong winter cooling over the Irminger Sea in winter 2014–2015, exceptional deep convection, and the emergence of anomalously low SST. *Geophysical Research Letters*, *43*(13), 7106–7113. https://doi.org/10.1002/2016GL069596

Dong, J., Fox-Kemper, B., Zhang, H., & Dong, C. (2021). The scale and activity of symmetric instability estimated from a global submesoscale-permitting ocean model. *Journal of Physical Oceanography*, *51*(5), 1655–1670. https://doi.org/10.1175/jpo-d-20-0159.1

Emanuel, K. A. (1994). Slantwise convection. In *Atmospheric convection* (pp. 392–417). Oxford University Press.

Ertel, H. (1942). Ein neuer hydrodynamischer Erhaltungssatz. *Naturwissenschaften*, *30*(36), 543–544. https://doi.org/10.1007/BF01475602

GEBCO Compilation Group (2020). GEBCO 2020 grid [Dataset]. https://doi.org/10.5285/a29c5465-b138-234d-e053-6c86abc040b9

Goldsworth, F. (2023). fraserwg/irminger-proj: v1.1 [Software]. Zenodo. https://doi.org/10.5281/zenodo.8233578

Goldsworth, F., Le Bras, I., Johnson, H., & Marshall, D. (2023). Data for "saturation of destratifying and restratifying instabilities during down front wind events: A case study in the Irminger Sea" [Dataset]. Zenodo. https://doi.org/10.5281/zenodo.8232682

Goldsworth, F. W. (2022). *Symmetric instability in the atlantic meridional overturning circulation*. Doctoral dissertation, University of Oxford. https://doi.org/10.5287/ora-xogpmrvzd

Griffies, S. M., & Hallberg, R. W. (2000). Biharmonic friction with a Smagorinsky-like viscosity for use in large-scale eddy-permitting ocean models. *Monthly Weather Review*, *128*(8), 2935–2946. https://doi.org/10.1175/1520-0493(2000)128⟨2935:bfwasl⟩2.0.co;2

Griffiths, S. D. (2003). Nonlinear vertical scale selection in equatorial inertial instability. *Journal of the Atmospheric Sciences*, *60*(7), 977–990. https://doi.org/10.1175/1520-0469(2003)060⟨0977:NVSSIE⟩2.0.CO;2

Gutjahr, O., Jungclaus, J. H., Brüggemann, N., Haak, H., & Marotzke, J. (2022). Air-sea interactions and water mass transformation during a katabatic storm in the irminger sea. *Journal of Geophysical Research: Oceans*, *127*(5), e2021JC018075. https://doi.org/10.1029/2021JC018075

Haine, T. W. N., & Marshall, J. (1998). Gravitational, symmetric, and baroclinic instability of the ocean mixed layer. *Journal of Physical Oceanography*, *28*(4), 634–658. https://doi.org/10.1175/1520-0485(1998)028⟨0634:gsabio⟩2.0.co;2

Hersbach, H., Bell, B., Berrisford, P., Hirahara, S., Horányi, A., Muñoz-Sabater, J., et al. (2020). The ERA5 global reanalysis. *Quarterly Journal of the Royal Meteorological Society*, *146*(730), 1999–2049. https://doi.org/10.1002/qj.3803

Hirschi, J. J., Barnier, B., Böning, C., Biastoch, A., Blaker, A. T., Coward, A., et al. (2020). The atlantic meridional overturning circulation in high-resolution models. *Journal of Geophysical Research: Oceans*, *125*(4), 1–35. https://doi.org/10.1029/2019JC015522

Hoskins, B. J. (1974). The role of potential vorticity in symmetric stability and instability. *Quarterly Journal of the Royal Meteorological Society*, *100*(425), 480–482. https://doi.org/10.1002/qj.49710042520

Jansen, M. F., Adcroft, A., Khani, S., & Kong, H. (2019). Toward an energetically consistent, resolution aware parameterization of ocean mesoscale eddies. *Journal of Advances in Modeling Earth Systems*, *11*(8), 2844–2860. https://doi.org/10.1029/2019MS001750

Josey, S. A., de Jong, M. F., Oltmanns, M., Moore, G. K., & Weller, R. A. (2019). Extreme variability in Irminger Sea winter heat loss revealed by Ocean Observatories Initiative mooring and the ERA5 reanalysis. *Geophysical Research Letters*, *46*(1), 293–302. https://doi.org/10.1029/2018GL080956

Le Bras, I. A.-A., Callies, J., Straneo, F., Biló, T. C., Holte, J., & Johnson, H. L. (2022). Slantwise convection in the Irminger Sea. *Journal of Geophysical Research: Oceans*, *127*(10). https://doi.org/10.1029/2022JC019071

Le Bras, I. A.-A., Straneo, F., Holte, J., & Holliday, N. P. (2018). Seasonality of freshwater in the East Greenland current system from 2014 to 2016. *Journal of Geophysical Research: Oceans*, *123*(12), 8828–8848. https://doi.org/10.1029/2018JC014511

Li, F., Lozier, M. S., Bacon, S., Bower, A. S., Cunningham, S. A., de Jong, M. F., et al. (2021). Subpolar north atlantic western boundary density anomalies and the meridional overturning circulation. *Nature Communications*, *12*(1), 3002. https://doi.org/10.1038/s41467-021-23350-2

Lozier, M. S., Li, F., Bacon, S., Bahr, F., Bower, A. S., Cunningham, S. A., et al. (2019). A sea change in our view of overturning in the subpolar North Atlantic. *Science*, *363*(6426), 516–521. https://doi.org/10.1126/science.aau6592

Marshall, J., Adcroft, A., Hill, C., Perelman, L., & Heisey, C. (1997). A finite-volume, incompressible Navier Stokes model for, studies of the ocean on parallel computers. *Journal of Geophysical Research*, *102*(C3), 5753–5766. https://doi.org/10.1029/96JC02775

Plougonven, R., & Zeitlin, V. (2009). Nonlinear development of inertial instability in a barotropic shear. *Physics of Fluids*, *21*(10). https://doi.org/10.1063/1.3242283

Prather, M. J. (1986). Numerical advection by conservation of second-order moments. *Journal of Geophysical Research*, *91*(D6), 6671–6681. https://doi.org/10.1029/JD091iD06p06671

Shu, R. (2023). Slantwise convection in the West Greenland current. In *21st Arctic-Subarctic ocean fluxes workshop*. Gran Canaria.

Smagorinsky, J. (1963). General circulation experiments with the primitive equations. *Monthly Weather Review*, *91*(3), 99–164. https://doi.org/10.1175/1520-0493(1963)091⟨0099:GCEWTP⟩2.3.CO;2

Spall, M. A., & Thomas, L. N. (2016). Downfront winds over buoyant coastal plumes. *Journal of Physical Oceanography*, *46*(10), 3139–3154. https://doi.org/10.1175/JPO-D-16-0042.1

Stamper, M. A., & Taylor, J. R. (2017). The transition from symmetric to baroclinic instability in the Eady model. *Ocean Dynamics*, *67*(1), 65–80. https://doi.org/10.1007/s10236-016-1011-6

Stone, P. H. (1966). On non-geostrophic baroclinic stability. *Journal of the Atmospheric Sciences*, *23*(4), 390–400. https://doi.org/10.1175/1520-0469(1966)023⟨0390:ONGBS⟩2.0.CO;2

Straneo, F., Kawase, M., & Pickart, R. S. (2002). Effects of wind on convection in strongly and weakly baroclinic flows with application to the Labrador Sea. *Journal of Physical Oceanography*, *32*(9), 2603–2618. https://doi.org/10.1175/1520-0485(2002)032⟨2603:EOWOCI⟩2.0.CO;2

Swingedouw, D., Houssais, M.-N., Herbaut, C., Blaizot, A.-C., Devilliers, M., & Deshayes, J. (2022). Amoc recent and future trends: A crucial role for oceanic resolution and Greenland melting? *Frontiers in Climate*, *4*. https://doi.org/10.3389/fclim.2022.838310

Talley, L. D., Pickard, G. L., Emery, W. J., & Swift, J. H. (2011a). Chapter 12 - Arctic ocean and nordic seas. In L. D. Talley, G. L. Pickard, W. J. Emery, & J. H. Swift (Eds.), *Descriptive physical oceanography* (6th ed., pp. 401–436). Academic Press. https://doi.org/10.1016/B978-0-7506-4552-2.10012-5

Talley, L. D., Pickard, G. L., Emery, W. J., & Swift, J. H. (2011b). Chapter 9 - atlantic Ocean. In L. D. Talley, G. L. Pickard, W. J. Emery, & J. H. Swift (Eds.), *Descriptive physical oceanography* (6th ed., pp. 245–301). Academic Press. https://doi.org/10.1016/B978-0-7506-4552-2.10009-5

Taylor, J. R., & Ferrari, R. (2009). On the equilibration of a symmetrically unstable front via a secondary shear instability. *Journal of Fluid Mechanics*, *622*, 103–113. https://doi.org/10.1017/S0022112008005272

Taylor, J. R., & Ferrari, R. (2010). Buoyancy and wind-driven convection at mixed layer density fronts. *Journal of Physical Oceanography*, *40*(6), 1222–1242. https://doi.org/10.1175/2010JPO4365.1

Thomas, L. N., & Lee, C. M. (2005). Intensification of ocean fronts by down-front winds. *Journal of Physical Oceanography*, *35*(6), 1086–1102. https://doi.org/10.1175/JPO2737.1

Thomas, L. N., Taylor, J. R., Ferrari, R., & Joyce, T. M. (2013). Symmetric instability in the Gulf stream. *Deep Sea Research Part II: Topical Studies in Oceanography*, *91*, 96–110. https://doi.org/10.1016/j.dsr2.2013.02.025

Walin, G. (1982). On the relation between sea-surface heat flow and thermal circulation in the ocean. *Tellus*, *34*(2), 187–195. https://doi.org/10.3402/tellusa.v34i2.10801

Yankovsky, E., & Legg, S. (2019). Symmetric and baroclinic instability in dense shelf overflows. *Journal of Physical Oceanography*, *49*(1), 39–61. https://doi.org/10.1175/JPO-D-18-0072.1